Highlights

Optimization of column layouts in buildings considering structural and architectural constraints

Yakov Zelickman, Oded Amir

- Gradient-based optimization of columns locations in arbitrary shaped floors.
- Thickness minimization with deflections, strength, and architectural constraints.
- Concrete savings may reach 50% with non-trivial optimized column locations.
- Even minor updates in traditional column layouts may result in significant savings.
- The trade-off between structural efficiency and architectural freedom is studied.

Optimization of column layouts in buildings considering structural and architectural constraints

Yakov Zelickman[a], Oded Amir[a]

[a]*Technion - Israel Institute of Technology, Haifa, 3200003, Israel*

Abstract

Reducing concrete consumption is important as part of the global effort of fighting the climate change, and specifically in concrete flat slabs as these are among the largest cement consumers. In this study we formulate an efficient gradient-based optimization of column locations, that minimizes the slabs' thickness with constraints on the deflections, bending moments and shear stresses while accounting for architectural considerations. The results show that the columns' optimal locations are not trivial and that the slab thickness is very sensitive to the columns' exact locations. Thus, concrete savings in slabs of up to 20% are possible with minor modification to traditional layouts of columns, and up to 50% with more pronounced updates, which emphasizes the importance of early collaboration between architects and engineers. The results indicate the critical trade-off between structural efficiency and architectural freedom and demonstrate the potential of formal optimization in structural design.

Keywords: Concrete floors, Structural optimization, Columns layout, Structural Engineering, Architectural constraints

1. Introduction

Concrete is one of the most highly consumed materials in the world, being the third largest source of carbon dioxide emissions [1]. Considering structural elements in buildings, a large portion of concrete is used in slabs. In fact, several recent studies investigated the usage of cement in different structural components in buildings and infrastructure, and it was shown that slabs hold the highest share of cement [2, 3, 4]. Therefore, reducing the volume of concrete in slabs has high potential for reducing

Email address: yzelick1@jhu.edu (Yakov Zelickman)

the environmental burden caused by cement production [4]. Moreover, slabs in buildings contribute significantly to the mass of the structure, and consequently to the gravitational and earthquake loads that the building must withstand. Thus, reducing the slabs' mass will lead to further concrete savings in other structural elements, such as columns and foundations.

Structural optimization is a design approach where a structural design problem is formulated as a constrained minimization problem and solved with mathematical programming tools [5]. It has been shown as an effective design tool in many branches of engineering that often leads to significant savings in material and improvements in performance [6, 7]. Thus, structural optimization is a promising design approach to reduce the environmental impact of concrete structures [4, 8, 9].

Optimization of concrete floor systems where the column locations are fixed, is the subject of many studies, aiming to minimize objective functions such as material consumption, cost, and environmental footprint. To name a few, Varaee and Ahmadi-Nedushan [10] minimized the cost of uni-directional flat plates with a single span, whereas cost minimization of flat plates with arbitrary shapes can be found in [11]. Cost optimization of a waffle slab was presented by Olawale et al. [12], who formulated a compact geometrical parametrization and therefore used a Genetic Algorithm (GA) for solving the optimization. Richer parametrization, that allows the shape of the ribs to vary was recently presented by Ismail and Mueller [13]. Some papers proposed optimization methods that consider multiple options for the floor structural system, for example [14].

The layout of columns, and more generally the layout of supports, significantly affects the structural response of plates. Therefore, optimizing the locations of the supporting elements is an effective way of reducing the environmental footprint of concrete slabs [15, 16]. In an early paper, the authors minimize the cost of a rectangular flat plate by optimizing a comprehensive set of parameters, including the span lengths [17]. Therein, a two-step framework is presented where the floor is optimized using GA for given span lengths, which are then updated following a heuristic scheme. Optimization of a rectilinear floor was presented in Shaw et al. [18], where the authors used GA to optimize the layout of prefabricated slab elements and the supporting columns. In a more recent study, the authors use Ant Colony Optimization to optimize the layout of an orthogonal-supported rectilinear building [19]. Additionally, the floor plan is optimized with a constraint on the total floor area. The objective function includes the cost of the frames and the slabs, and the eccentricity between the mass- and the rigidity- centers. Recently, Building Information Modelling (BIM) was coupled with Finite Element (FE) analysis and GA to create a framework for preliminary design of concrete structures, including spacing between column grid-lines [15]. In another recent study, the authors use Monte Carlo method to find the optimal locations of supports of concrete plates, minimizing the strain energy, reinforcement steel and maximal deflection [20].

All studies that were mentioned so far, and most of the available literature that discusses optimization of concrete floor systems, adopts meta-heuristic and zero-order optimization algorithms, which allow to cope with the non-differentiable and discontinuous constraints, but also becomes very expensive computationally in high dimensional optimization [21]. Therefore, the design space includes a small number of design variables, restricting the optimization to regular layouts of columns or to a limited number of columns.

Gradient-based optimization algorithms are more likely to converge to local minima than meta-heuristic algorithms, but offer superior numerical efficiency and therefore were also considered in many studies. In a straightforward approach for optimization of supports' locations, the coordinates of the supported nodes are being optimized [22, 23]. This approach requires constant remeshing and control over the FE mesh, and therefore is numerically expensive and may encounter stability issues. Another approach, that uses a SIMP-like parametrization, was proposed by Buhl [24]. Mathematical continuity is obtained by adding springs to all nodes and assigning penalized topological design variables to each one of the springs. Thus, by adding a constraint on the sum of the topological design variables, the most effective springs remain, designating the optimal locations. This approach was adopted in several studies, for example Jihong and Weihong [25], Denli and Sun [26], and recently used by Meng et al. [27] to minimize the compliance of plate roof structures. In a recent paper by the authors we introduce the stiffness projection method for support location optimization, which is both numerically efficient and mesh-independent, and therefore much less prone to convergence to local minima than the other gradient-based approaches [28]. Similarly to Meng et al. [27], the optimization formulation there is purely academic, where unconstrained compliance minimization was adopted for the purpose of establishing the stiffness projection method.

From the discussion above it is apparent that existing studies on column layout optimization of concrete floors were using meta-heuristic algorithms, mainly GA. As a result, the design space is limited to a small number of design variables, and therefore the existing methods focus on a regular grid of columns and simple floor plans. In most examples, architectural constraints were not considered, or they were limited to restricting the span length of the regular grid of columns. On the other hand, studies that used efficient gradient-based algorithms, which result in a rich design space, consider only global structural performance and lack the necessary structural and architectural constraints for the design of concrete floors.

In this study we aim to fill this gap by proposing a gradient-based optimization for the layout of the columns in floors with arbitrary shapes, considering the major structural design requirements of concrete plates as well as imposing general architectural-geometrical constraints. In this regard we note that the focus of the paper is on residential and office buildings, however other types of buildings and floor systems can be considered as well with appropriate load conditions, and structural models for the slab. Additionally, we investigate the sensitivity of the plate thickness to the locations of columns.

Specifically, we build off the stiffness projection method that was presented in the authors' previous work [28], and extend it significantly by adding deflection, punching shear, bending moment, and architectural constraints, as well as adding the plate thickness to the design space and explicitly minimizing the concrete volume. As a result, the columns are not restricted to any location or pattern (other than the architectural constraints), which gives rise to non-trivial layouts and significant reduction in concrete mass. As expected, there is a clear trade-off between concrete volume and the architectural design freedom. Less expected is how significant are the concrete savings when only mild changes are made to the column locations, imposing only minor compromise on the architectural design. This study demonstrates the importance of close collaboration between structural engineers and architects from the preliminary design stages [18], when the column locations are determined.

The remainder of this paper is arranged as follows. In the next section we briefly present the mathematical model, thereafter in Section 3 we discuss the optimization formulation extensively. In Section 4 we present three numerical examples that are followed by a brief discussion and some concluding remarks in Section 5. The paper has two appendices: The first presents the analytical sensitivity analysis and the second provides some details about the implementation of the optimization method.

2. Mathematical model

In structural optimization, the mathematical model is a structural model that predicts the structural response to a given set of loads for a given set of parameters, including the design parameters. In the context of the current study, the structural model is a plate model where the supports locations and the thickness may vary throughout the optimization. We note that the mathematical model that we use in the current study was already presented and discussed extensively in our previous work [28]. Herein the mathematical model is described briefly for completeness.

The slabs are modeled with plate finite elements using Mindlin plate theory [29, 30]. Following common practice in the analysis of concrete slabs, we assume small displacements and strains as well as linear elastic behavior of the concrete. Thus, the floor is modeled with 4-noded plate elements with mixed interpolation, that are known to be accurate and insensitive to shear locking [31].

Since we optimize the locations of the columns, the boundary conditions of the slab change throughout the optimization. Generally, this class of problems suffers from several difficulties: 1) Possible discontinuity of the design space; 2) High computational cost if remeshing is used; and 3)

Tendency to converge to poor local optima. Therefore, in this study we use the stiffness projection method that was presented in our previous work to overcome these challenges [28].

As the name suggests, the basic idea is to project the stiffness of the columns upon the plate's FE mesh instead of modeling the columns explicitly. Thus, all nodes within a circular projection area Ω_i defined by a projection radius of η_i, have added nodal stiffness. This added stiffness equals to the column's stiffness matrix multiplied by a weight factor w_{ij} that relates the i^{th} column with the j^{th} node. Thereafter, the added nodal stiffness matrices are assembled into a global equivalent stiffness matrix of the i^{th} column

$$\mathbf{K}_{cp,i} = \sum_{\Omega_i} w_{ij} \mathbf{K}_{c,i} \quad \text{with} \quad \Omega_i = \left\{ j | r_{ij} \leq \eta \right\}. \tag{1}$$

In the above expression, $\mathbf{K}_{cp,i}$ and $\mathbf{K}_{c,i}$ are the i^{th} column equivalent and nominal stiffness matrices; r_{ij} is the distance between the i^{th} column and the j^{th} node; and the sum operator represents assembly according the degrees of freedom of the model. Because we use gradient based optimization in this study, all functions have to be differentiable and therefore we use a smooth radial super-Gaussian function for the projection weight factors

$$\tilde{w}_{ij} = \tilde{w}\left(r_{ij}\right) = \exp\left(-0.5\left(\frac{r_{ij}}{\eta}\right)^{2\beta}\right), \tag{2}$$

where β is a parameter that controls the sharpness of the transition across the boundary of the projection area. This means that mathematically the stiffness of any column is projected onto all nodes of the FE mesh, with practically zero projection weight outside the desired projection area. To ensure that no excess stiffness is generated by the projection, we normalize the projection weights

$$w_{ij} = \frac{\tilde{w}_{ij}}{\sum_k \tilde{w}_{ik}} \quad \text{with} \quad k = [1 \ldots N_n], \tag{3}$$

where N_n is the total number of nodes. After the equivalent stiffness matrices of all columns have been computed, they are added to the plate's stiffness matrix $\mathbf{K}_p$, which results in the stiffness matrix of the supported plate, $\mathbf{K}$. Finally, walls are modeled as pinned supports that are added to all nodes within the projection area of the walls on the FE mesh. To ensure that all walls are modeled, in all examples we use regular FE meshes with element size that is less than the wall thickness.

3. Optimization problem formulation

In this section we present the proposed design-oriented problem formulation. Thus, we minimize the concrete volume, consider the major service and design limit state requirements, as well as adding architectural constraints (AC). Arranging the optimization problem into standard form, we obtain

$$\begin{aligned}
\underset{\mathbf{X}}{\text{minimize}} \quad & f_0 = V \\
\text{s.t.} \quad & f_1 = \frac{\tilde{\delta}}{\tilde{\delta}^*} - 1 \leq 0 \\
& f_2 = \frac{\tilde{\sigma}_{ts}}{\tilde{\sigma}^*_{ts}} - 1 \leq 0 \\
& f_3 = \frac{\tilde{\mu}}{\tilde{\mu}^*} - 1 \leq 0 \\
& \tilde{\mathbf{X}} \in \Omega_{arc} \\
\text{with:} \quad & \mathbf{K}\mathbf{u}_{\mathrm{s}} = \mathbf{f}_{\mathrm{s}} \\
& \mathbf{K}\mathbf{u}_{\mathrm{d}} = \mathbf{f}_{\mathrm{d}}.
\end{aligned} \tag{4}$$

In the formulation above: f_1, f_2 and f_3 are respectively the deflection, shear stress, and bending moment constraints. The next set of constraints are the architectural constraints, which are imposed through the design space definition. The last two expressions represent the equilibrium equations that are considered in a nested configuration. Although the formulation is general and any number of load cases can be accommodated, in this study all examples have only two different load cases with uniformly distributed loads that correspond to service and design limit states. The service limit state and the design limit state load vectors, $\mathbf{f}_s$ and $\mathbf{f}_d$, are given by

$$\begin{cases} \mathbf{f}_s = \mathbf{g} + \Delta\mathbf{g} + \mathbf{q} \\ \mathbf{f}_d = 1.4\,(\mathbf{g} + \Delta\mathbf{g}) + 1.6\mathbf{q} \end{cases},$$

where $\mathbf{g}$, $\Delta\mathbf{g}$ and $\mathbf{q}$ are the nodal self weight, dead load, and live load vectors, respectively. We note that including pattern loading would represent the expected loads on the floor more accurately. However, the optimized design will be influenced only marginally by a pattern loading, because different load patters balance each other in the context of the optimal location of the columns. Furthermore, in residential buildings as well as in most office buildings, the live loads are much smaller than the dead loads, diminishing the effect of pattern loading. Finally, as will be apparent from the results, the optimized designs tend to have even column distribution, and therefore the effect of pattern loading is even smaller. In fact, under such circumstances some building codes do not require to consider pattern loading [32, 33].

The plate forces and moments are obtained in design limit state by computing

$$\hat{\mathbf{S}} = \mathbf{D}\mathbf{B}\mathbf{u}_d, \tag{5}$$

where $\hat{\mathbf{S}}$ is a vector with the plate forces and moments evaluated at the Gauss points, $\mathbf{D}$ is the plate's constitutive matrix, and $\mathbf{B}$ is a differentiation matrix. The nodal forces and moments are computed using the SPR technique [34]

$$\mathbf{S} = \left\{\mathbf{M}_{xx}^T \quad \mathbf{M}_{yy}^T \quad \mathbf{M}_{xy}^T \quad \boldsymbol{\sigma}_{xz}^T \quad \boldsymbol{\sigma}_{yz}^T\right\}^T = \mathbf{W}^T\hat{\mathbf{S}}, \tag{6}$$

where $\mathbf{S}$ is a vector with the nodal bending moments and transverse shear forces, and $\mathbf{W}$ is a constant transformation matrix. Finally, $\mathbf{X}$ is the normalized *mathematical* design vector, whereas $\tilde{\mathbf{X}}$ is the *physical* design vector that holds the actual design parameters that we wish to optimize.

3.1. Architectural design space

Due to the explicit parametrization, in which the coordinates of the column locations are considered as design variables, architectural-geometrical limitations may be introduced by appropriate definition of the design space. This inherently ensures that the architectural requirements are met while exploring the design space, hence the title Architectural Design Space. However, for brevity we will refer to the architectural designs space, simply as the design space. Another advantage of considering the architectural requirements through the design space is that they do not have to be differentiable, which increases the range of architectural constrains that can be imposed.

Thus, the architectural constraints (AC) in Eq. (4) are imposed through the design space definition, $\tilde{\mathbf{X}} \in \Omega_{arc}$, where Ω_{arc} is a set of all architecturally admissible designs. This set encodes the specific architectural requirements for a design problem and defines the allowable range for each design variable. Considering a floor that is supported on N_{col} columns, the design variables vector is

$$\tilde{\mathbf{X}}^T = \left[\mathbf{x}_c^T, \mathbf{y}_c^T, h\right]. \tag{7}$$

where, $\mathbf{x}_c$ and $\mathbf{y}_c$ are vectors with the x and y coordinates of the columns and h is the thickness of the slab. Accordingly, the design space has $N_{dv} = 2N_{col} + 1$ design variables, and the admissible set Ω_{arc} has the same dimension.

The limits of the thickness design variable are straightforward: $h_{min} \leq h \leq h_{max}$, where h_{min} arises from structural building codes and regulations, and h_{max} is an architectural parameter, defining the available space for the structural slab. However, for general floors with non-convex contours and arbitrary geometrical-architectural constraints, the limits of the column locations variables are design-dependent and therefore more complex. In this regard, we distinguish between the trivial AC that ensure that the columns remain within the floor area, and the characteristic AC that represent all the additional requirements, such as restricting a column movement to a specific region. As in general constrained optimization, not all constraints must be active and a characteristic AC usually will make the corresponding trivial AC inactive.

Considering the trivial AC, we require that at each design iteration, the updated location of a column will remain in the circle defined by the current location of the column and the shortest distance to the boundary, which includes both the contour of the floor and the openings. Therefore, for a column with shortest distance of d_{min}, the design limits in each direction are conservatively set to $\frac{d_{min}}{2}$, which results in the following limits

$$\left[\mathbf{x}_{c,max}, \mathbf{x}_{c,min}\right] = \mathbf{x}_c \pm \frac{1}{2}\mathbf{d}_{min}\left(\mathbf{x}_c, \mathbf{y}_c\right) \tag{8}$$

$$\left[\mathbf{y}_{c,max}, \mathbf{y}_{c,min}\right] = \mathbf{y}_c \pm \frac{1}{2}\mathbf{d}_{min}\left(\mathbf{x}_c, \mathbf{y}_c\right), \tag{9}$$

where $\mathbf{d}_{min}$ is a vector with the shortest distance from all columns to the boundary of floor.

To compute d_{min} we discretize the floor boundaries to sampling points (SP) with spacing of roughly $0.1\,[m]$ between adjacent SP. Thereafter, we compute the distance from the column to all SP, select the two closest SP, and approximate d_{min} with shortest distance to the line connecting both SP. Additionally, we use the derivatives of the shortest distance with respect to the column coordinates to identify the direction to the nearest boundary. For example, considering the x coordinate of a column, a positive derivative indicates that the closest SP is somewhere to the left of the column location. Therefore, the design limit to the right may be larger and is defined by the maximal move limit value, which is discussed in Appendix B.2. Similar logic applies also to a negative sign of the derivative and when considering the y coordinate. We note that in a case of close vicinity of a column to an ear vertex of the boundary polygon, the proposed strategy may allow the column to exit the domain. However, since the columns naturally prefer to remain strictly within the floor area, setting small enough distance between the SP resolves any related issues.

The characteristic AC represent additional limitations on the column locations. In engineering practice it is often that the multidisciplinary design is performed sequentially. Thus, first an architect designs the functionality and the layout of the partitioning walls, and then the location of the columns are defined by the structural engineer along those walls. Therefore, one class of characteristic AC are path constraints, where for a given column we define a path along which it is allowed to move. From a mathematical perspective, each column is assigned with a scalar parameter t_i, and both coordinates of the column are defined by explicit path functions, which encode the allowed path: $x_{c,i} = x_{c,i}(t_i)$ and $y_{c,i} = y_{c,i}(t_i)$. In section 4.2 we will present example of path constraints. A natural extension of the path constraints are areal constraints, where the columns are allowed to move only within a predefined

2D subdomain. We will use such areal constraints in Section 4.3 to investigate the relation between the design freedom and the concrete savings.

As mentioned, we distinguish between the *physical design variables*, which refers to the actual parameters that we want to find, and the *mathematical design variables*, that we solve in the optimization problem

$$\mathbf{X}^T = \left[\mathbf{r}_c^T, \mathbf{s}_c^T, \omega\right]. \tag{10}$$

The mathematical design variables are normalized and linearly related to the physical design variables

$$\mathbf{X} = \mathbf{N}\tilde{\mathbf{X}}, \tag{11}$$

where $\mathbf{N}$ is the diagonal normalization matrix. The entries on the diagonal of $\mathbf{N}$ are $1/B_x$, $1/B_y$, or $1/(h_{max} - h_{min})$ for the column locations in x and y directions, and the slab thickness, respectively. This normalization generally results in more stable optimization and conveniently separates the optimization procedure from the specific geometrical parameters of the problem being solved. The limits on the mathematical design variables are obtained by normalization of the physical design limits.

3.2. Volume Objective function

As stated, we wish to minimize the concrete consumption, and therefore minimize the concrete volume. We measure the concrete volume by summing the volumes of the individual finite elements

$$V = \sum_{\ell=1}^{N_\ell} hA_\ell, \tag{12}$$

where A_ℓ is the area of the ℓ^{th} finite element, and N_ℓ is the total number of elements in the FE mesh.

3.3. Deflection Constraint

Many standards define the allowed deflection in concrete elements as a fraction of their span. In general, floors have multiple spans, each possibly with different length, and therefore different areas of a floor might have different allowed deflection. To successfully impose deflection constraints we define the relative deflection at each node δ_j as the ratio between the actual elastic downward deflection in service limit state and the allowed deflection at this node

$$\delta_j = \frac{w_j}{w_{A,j}}, \tag{13}$$

where w_j and $w_{A,j}$ are the actual and allowed deflections in z direction at the j^{th} node, respectively. The constraint aggregates all nodal relative deflections by considering the maximal relative deflection, which is approximated using a p-norm function

$$\tilde{\delta} = \left(\sum_{j=1}^{N_n} \delta_j^p \right)^{\frac{1}{p}}. \tag{14}$$

In the equation above, $\tilde{\delta}$ is the approximate maximal relative deflection, N_n is total number of nodes in the FE mesh, and p is an even number allowing to account for both positive (upward) and negative (downward) deflections. Moreover, since the deflections surface is smooth, we use high power value of $p = 30$. This approximation overestimates the real maximum, $\tilde{\delta} > \max(\boldsymbol{\delta})$, which may lead to undesired conservativeness. Therefore, the threshold value of the constraint is dynamically updated as follows

$$\tilde{\delta}^* = \frac{\tilde{\delta}}{\max(\boldsymbol{\delta})} \delta^*, \tag{15}$$

every $N_{Ic} = 5$ iterations, where the nominal required relative deflection is $\delta^* = 1.0$.

The definition of the allowed deflection follows the recommendations in Eurocode 2 (EC2) [32], where the long term deflection should be less than $\frac{1}{250}$ of the span length. Thus, assuming a long term deflection coefficient of 3.0, the allowed deflection at node j is

$$w_{A,j} = \frac{L_{eq,j}}{750}, \tag{16}$$

where $L_{eq,j}$ is the equivalent span length at this node.

In a traditional approach for obtaining the span lengths in irregular floors, the spans are identified by manual inspection of the deflection surface, and then the span lengths are set as the diameter of the maximal inscribed circle in each span. However, since the columns change their locations throughout the optimization, it is not clear how to identify the irregular spans in a systematic and differentiable manner. Therefore, we take a slightly different approach and directly approximate this diameter as $d = \sqrt{2} r_{min}$, where r_{min} is the distance to the closest column or wall. This approximation is equivalent to the traditional approach for regular and rectangular spans, and conservative otherwise. Thus, we define the equivalent span length at any node j as follows,

$$L_{eq,j} = r_0 + \sqrt{2} r_{min,j} \quad \text{with} \quad r_{min,j} = \min_i \left(r_{ij} \right), \quad i \in [1, \ldots, N_{col} + N_{wall}], \tag{17}$$

where $r_{min,j}$ is the distance from the j^{th} node to the closest column or wall and r_0 is a constant value that we add to allow some minimal deflection at the supports. This allowed deflection at the columns is necessary to accommodate for the inevitable deflection at the supports, as the supports have finite stiffness, as discussed in Section 2. We chose the value $r_0 = 0.7\,[m]$, which allows an elastic deflection at the supports of approximately $1 \times 10^{-3}\,[m]$. Finally, we approximate the non-differentiable distance to the closest column in Eq. (17) with a p-norm function

$$r_{min,j} \approx \left(\sum_i^{N_{col}+N_{wall}} r_{ij}^{-p} \right)^{-\frac{1}{p}}. \tag{18}$$

3.4. Shear Constraint

Shear in slabs, or punching shear, is a key consideration in the design of concrete slabs and hence is added to the formulation. We define a sufficient thickness of the slab such that the punching resistance at each point can be provided by steel details only, without further thickening. Thus, following the recommendations in EC2, we will require for each node j that

$$\begin{cases} \sigma_{xz,j} \leq v_{Rd,max} \\ \\ \sigma_{yz,j} \leq v_{Rd,max} \end{cases} \quad \text{with} \quad v_{Rd,max} = 0.4 \cdot 0.6 \left[1 - \frac{f_{ck}}{250} \right] f_{cd} \approx 0.2 f_{cd}. \tag{19}$$

In the expression above, $\sigma_{xz,j}$ and $\sigma_{yz,j}$ are the plate transverse shear stresses acting at node j in design limit state, $v_{Rd,max}$ is the maximal allowed shear stress, f_{ck} and f_{cd} are the characteristic and compression design strengths of the concrete (in $[MPa]$). We note that we omit the eccentricity parameter β suggested by the EC2 [32], because the shear stresses are computed directly and thus the actual structural response is already taken into account. Similarly to the deflection constraint, we constrain the maximal shear stress rather than having separate nodal constraints. Thus, the approximate maximal shear stress is

$$\tilde{\sigma}_{ts} = \left(\sum_{j=1}^{2N_n} \sigma_{ts,j}^{p} \right)^{\frac{1}{p}} \quad \text{with} \quad \boldsymbol{\sigma}_{ts} = \begin{bmatrix} \boldsymbol{\sigma}_{xz} \\ \boldsymbol{\sigma}_{yz} \end{bmatrix}. \tag{20}$$

We note that the shear may be both positive and negative and therefore the value of the power p should be even. The threshold is updated in the same way as in the deflection constraint,

$$\tilde{\sigma}_{ts}^{*} = \frac{\tilde{\sigma}_{ts}}{\max(\boldsymbol{\sigma}_{ts})} v_{Rd,max}. \tag{21}$$

For convenient presentation of the results, we define the relative shear stress as the ratio between the nodal shear stress and the maximal allowed shear stress

$$\boldsymbol{\tau}_{xz} = \frac{\boldsymbol{\sigma}_{xz}}{v_{Rd,max}}, \quad \boldsymbol{\tau}_{yz} = \frac{\boldsymbol{\sigma}_{yz}}{v_{Rd,max}}. \tag{22}$$

3.5. Bending Moment Constraint

Another important design consideration in concrete elements is the bending moment capacity. In slabs, it is common that no compressive steel is needed. Thus, in this study we aim for structural depth that will subsequently allow a design with tensile steel only. Following recommendations in many design codes including EC2 [32] and ACI[33], we assume a simplified rectangular stress block with maximal height of $0.4d$, where $d = h - d_s$ is the effective structural depth and d_s is the concrete cover of the steel rebars. Thus, the maximal bending capacity per unit width, without compression rebars is given by

$$M_c = 0.32\,(h - d_s)^2 f_{cd}, \tag{23}$$

which provides good approximation for $f_{cd} \leq 28[Mpa]$, especially as the moments approach M_c.

Following common practice, we take into account the torsion moments in the slab by considering the Wood and Armer (W&A) moments [35]. Thus, we combine the pure bending moments with the torsional moments to create the design moments

$$M_{rx,max} = M_{xx} + |M_{xy}|$$
$$M_{rx,min} = M_{xx} - |M_{xy}|$$
$$M_{ry,max} = M_{yy} + |M_{xy}|$$
$$M_{ry,min} = M_{yy} - |M_{xy}|,$$

where M_{xx}, M_{yy}, M_{xy} are the plate moments in design limit state. For convenient presentation of the bending of the plate, we define the relative moment as the ratio between the nodal moments and the moments capacities. Thus, the relative $M_{rx,max}$ moment at any node j is

$$\mu_{rx,max,j} = \frac{M_{rx,max,j}}{M_c}, \tag{24}$$

and similarly for the other moments. In order to constrain all moments at all nodes, we constrain the approximate maximum relative moment

$$\tilde{\mu} = \left(\sum_{j=1}^{4N_n} \mu_j^p\right)^{\frac{1}{p}} \quad \text{with} \quad \boldsymbol{\mu} = \begin{bmatrix} \boldsymbol{\mu}_{rx,max} \\ \boldsymbol{\mu}_{rx,min} \\ \boldsymbol{\mu}_{ry,max} \\ \boldsymbol{\mu}_{ry,min} \end{bmatrix}. \tag{25}$$

Finally, the threshold value of the moment constraint is updated similarly to the shear and deflection constraints, with normalized desired threshold value $\mu^* = 1$

$$\tilde{\mu}^* = \frac{\tilde{\mu}}{\max(\boldsymbol{\mu})}. \tag{26}$$

3.6. Optimization Sequence

It was observed during our numerical experiments that often only the displacement constraint is active. Thus, in many cases the bending moment constraint and the shear constraint may be omitted. This results in much faster optimization because it spares computing $\mathbf{u}_d$ as well as the corresponding adjoint vectors, each requires solving a set of equilibrium equations which is the most expensive computational task. Obviously, one cannot know in advance whether the design limit state constraints will be active. Therefore, in this study we implemented a hierarchical optimization sequence. Initially, we optimize only with the displacement constraint and check upon convergence the resultant moment and shear distribution. In a case that both the moment and shear values are within the desired limits, the optimized design is considered as the solution of the optimization problem. Otherwise, we update the optimized design by another optimization. This time, all constraints are included and the initial design is the optimized design from the previous optimization.

3.7. Sensitivity analysis

In this study we use gradient-based optimization that allows to effectively cope with multidimensional optimization, and specifically we adopt the MMA algorithm [36]. Therefore, the derivatives of all functionals in Eq. (4) with respect to all design variables should be derived, a process that is often referred to as Sensitivity Analysis (SA). The SA of a functional f_i with respect to the *mathematical* design variables is given by

$$\frac{\partial f_i}{\partial \mathbf{X}} = \frac{\partial f_i}{\partial \tilde{\mathbf{X}}}\mathbf{N}^{-1} \tag{27}$$

where $\frac{\partial f_i}{\partial \tilde{\mathbf{X}}}$ are the derivatives with respect to the *physical* design variables, and presented in detail in Appendix A.

4. Numerical examples

In this section we demonstrate the ability of the proposed method to reduce concrete volume in slabs by optimizing the column locations. Additionally, the results presented here demonstrate the critical trade-off between the structural efficiency and the architectural cost and emphasize the importance of collaboration between architects and engineers at early stages of the project. The first example is a simple design problem that validates the proposed optimization method, illustrates the sensitivity of the slab thickness to the exact column location, and shows that the optimal location of columns might be non-intuitive. The other two examples are inspired by real projects with more complicated geometries and demonstrate the ability of the proposed method to contribute to concrete savings in complex, real-life projects while satisfying the architectural requirements. Furthermore, we take advantage of the more realistic geometries to investigate the effects of the design freedom on the concrete savings.

Table 1. Material properties and other design parameters used in the current study

symbol	value	units	description
d_s	0.025	[m]	concrete cover
f_{cd}	17.40	$[MPa]$	concrete compression design strength
E	30000	$[MPa]$	concrete modulus of elasticity
ν	0.3	[-]	concrete Poisson's ratio
γ	$5/6$	[-]	shear strain correction factor
Δg	4	$[kN/m^2]$	dead load
q	1.5	$[kN/m^2]$	live load
γ_c	25	$[kN/m^3]$	concrete weight density

In all designs presented in this section, the deflection constraint is active. In fact, we see that the deflections often reach the allowed values in many regions, indicating better utilization of the feasible space and hence better design. Therefore, we introduce the mean relative deflection $\bar{\delta}$ as an additional measure of the optimality, providing another basis for comparison between different designs, where higher $\bar{\delta}$ values indicate better designs. Furthermore, we use $\bar{\delta}$ also as an absolute gauge of the optimality, where we first need to establish the maximal possible value that corresponds to the best design. In this regard, we note that since the deflection surface is smooth, whereas the allowed deflection surface is an intersection of cones and planes, $\bar{\delta} = 1.0$ cannot be reached. To assess the actual best design in terms of the deflection we recall that the slope of the deflected surface should be zero above the optimal location of the supports, as has been shown in other studies dealing with supports optimization, for example [37, 28]. Thus, we can estimate the maximal theoretical mean relative deflection, $\bar{\delta}_{max}$, by considering representative cases of fixed-fixed and cantilever beams, which have known analytical deflection curves. Following the reasoning in Section 3.3, we set linear allowed deflections functions with zero value at the supports, integrate the relative deflections along the representative beams, and divide by their lengths, which yields $\bar{\delta} \cong 0.77$ and $\bar{\delta} \cong 0.64$, respectively. Therefore, we can assume that $\bar{\delta}_{max} \in [0.64, 0.77]$.

4.1. Example 1: Single Column Optimization

In the first example we wish to validate the optimization method, demonstrate that the optimal location of columns might not be trivial, and illustrate the sensitivity of the slab thickness to the column location. For this purpose we consider a minimalist problem and assume no architectural constraints, which together allow us to explore the entire design space. Thus we optimize a single column in an apartment located in a typical residential tower. The floor plan and all dimensions are plotted in Figure 1a, where the columns have square cross section with $0.35[m]$ side lengths. In addition to the column being optimized, the boundary conditions of the floor include seven columns along the contour of the floor, symmetry boundary conditions along the inner edges, and a portion of an internal core with wall thickness of $0.25[m]$. The floor is discretized with $0.24 \times 0.24[m]$ elements and is subjected to additional external loads as listen in Table 1. The design space includes the coordinates of the column, which can be anywhere within the apartment, as marked by the hexagonal pattern in Figure 1a, and the thickness of the slab h, which may vary between $h_{min} = 0.05[m]$ and $h_{max} = 0.5[m]$.

The optimized column location is $(x_c, y_c) \approx (10.3, 5.6)[m]$ and the corresponding slab thickness is $h = 0.228[m]$, with concrete volume of $V = 49.9 \left[m^3\right]$. This optimized design, as well as the resultant deflections w, the allowed deflections w_A, and the relative deflection δ, are presented in Figures 1b, 1c and 1d, respectively. Inspecting these figures, it is evident that the deflection constraint is active, with the maximal deflection at the resultant three spans reaching the maximal allowed deflection,

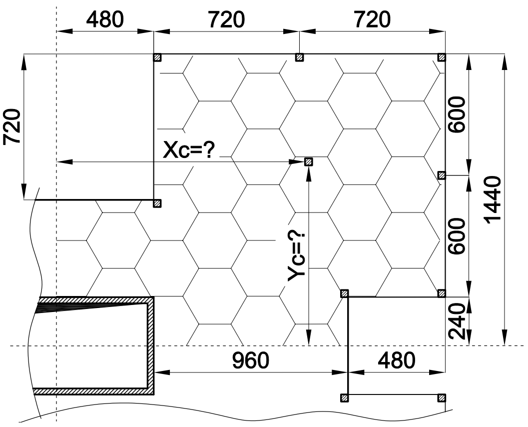

(a) Floor plan, all dimensions in $[cm]$

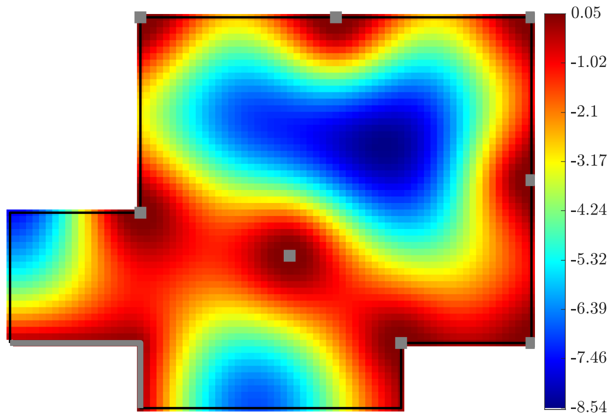

(b) Deflections $w\,[mm]$

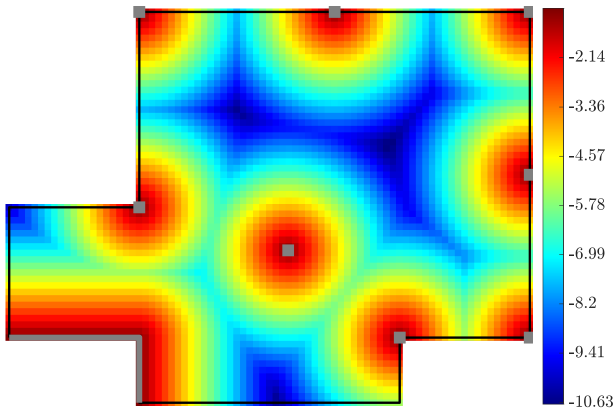

(c) Allowed deflections $w_A\,[mm]$

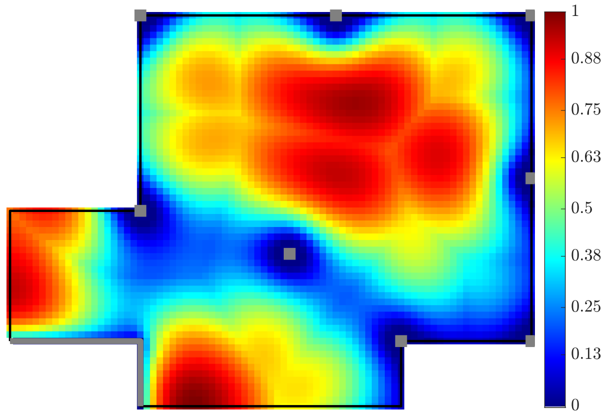

(d) relative deflections δ

Fig. 1. Problem setup for the single column optimization, optimized column location and the resultant deflections maps. The deflection constraint is active with deflections in all three spans reaching the allowed deflection values.

hence utilizing effectively the feasible space with $\bar{\delta} = 0.516$. Figure 2a presents the distribution of the minimal relative moment in y direction, where $-0.833 \leq \mu_{ry,min} \leq 0.278$ indicating that $\mu_{ry,min}$ is within the allowed range. In fact, this is true for all normalized moments and shear stresses, which have similar distributions and yields extremum values of $\mu_{min} = 0.8706$, $\mu_{max} = 0.3645$, and $\tau_{ts,max} = 0.985$. Thus, following the discussion in Section 3.6, re-optimization with all constraints was not necessary.

Once the optimized column location has been found, we verify it by manually investigating the entire design space. Thus, we generate an optimal surface by finding the minimum required slab thickness for every column location. We discretize the design space of the column location to a grid of $0.3 \times 0.3[m]$ points and minimize the slab thickness for a column fixed at each one of those grid

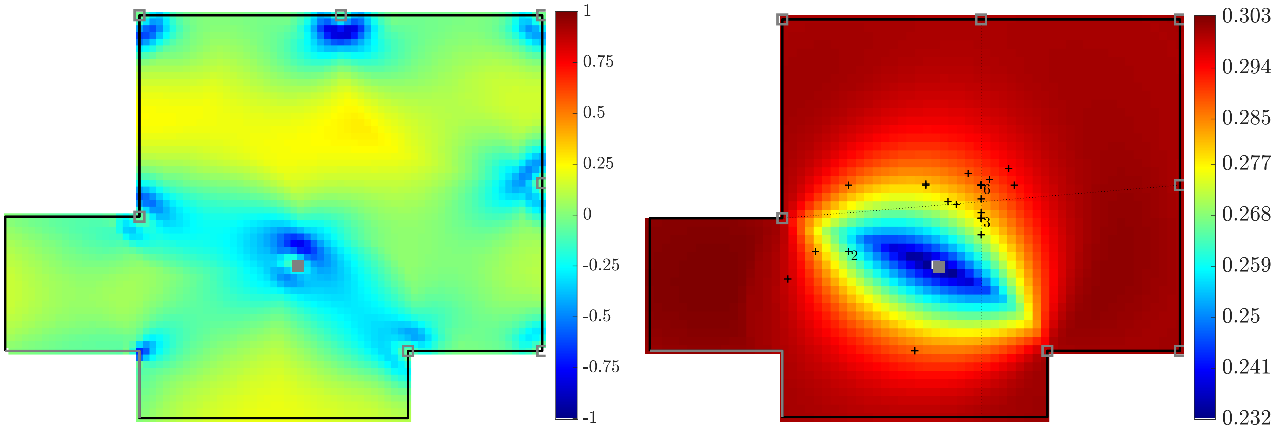

(a) $\mu_{ry,min}$

(b) Optimal thickness surface, $h\ (x_c, y_c)\ [m]$

Fig. 2. (a) Normalized minimal moment in y direction, showing that $\mu_{ry,min}$ is feasible. (b) Investigation of the entire design space of (x_c, y_c). Each pixel is $0.3 \times 0.3\ [m]$ and represents the required slab thickness $h[m]$ for each column location, with minimal value of $h = 0.2322\ [m]$. The optimized location of the column is at the region with the minimal required thickness, implying successful convergence to the optimum. The black crosses are the suggested locations for the column, as obtained by 26 practicing structural engineers, and show that the optimal column location is not trivial.

points. Figure 2b presents the optimal surface, where the color of each pixel represents the required slab thickness for a column located at the centre of the pixel. The filled gray square is the optimized column location as obtained from the straightforward optimization and it is evident that it is located at the optimum. In fact, the minimal required thickness obtained by the optimization is slightly smaller than the minimal value obtained by the design space exploration, probably due to the continuous nature of the design variables $[x_c, y_c]$.

The optimal location of the column is not intuitive, as a more traditional solution would be to locate the column closer to the center of the large span. To test this hypothesis we performed a poll among 26 practicing structural engineers and asked them where would they locate the column, ignoring any architectural considerations. The black crosses in Figure 2b represent the answers received from the participants of the poll, where the numbers indicate multiple answers for a certain location. It can be seen that most participants located the column approximately at the center of the large bay, marked by the intersection of the dotted grid lines. These results confirm that the optimal column location might not be obvious, even in a simple floor geometry and without considering any architectural constraints.

For each column location suggested by the participants of the poll, we computed the required slab thickness, which vary between $h_{ref} \in [0.2688, 0.2987][m]$ with mean value of $\bar{h}_{ref} = 0.2823[m]$. Thus, we can say that the concrete savings vary between 0% in the unlikely case that the column was originally located at the most efficient location, and 23.8% when considering $\bar{h}_{ref}$. Moreover, inspecting the optimal thickness surface in Figure 2b, it seems that it has steep gradient values around the optimal point, such that moving the column by one pixel, or $0.3[m]$ (in the correct direction), results in thickness reduction of almost $10[mm]$. This implies a high sensitivity of the slab thickness to the column location, at least in regions with large gradients of the optimal thickness. In the current example, this region reaches the traditional location of the column and includes most of the suggested locations in the poll. Thus, indicating that significant savings could be achieved even with small changes to a traditional design.

4.2. Example 2: Rounded Triangular Floor

The second example that we present is inspired by a floor plan of an actual building that was presented in [38] in the context of post-tensioning optimization. Therefore, this example shows the ability of the proposed method to deal with real-life problems characterized with many columns as well as non-convex shapes of floors. Furthermore, we add path constraints to ensure that the design comply with an architectural design of this floor plan.

The floor has a triangular shape with rounded corners, has three rectangular openings, and supported on 19 square columns as well as a central concrete core. The thickness of the core walls is $0.35[m]$ and therefore the floor is modeled with slightly smaller square FE, with $0.333[m]$ side length. All other parameters are the same as in the previous example. Figure 3a depicts the floor plan and some measures, whereas all geometrical data can be found in the Supplementary Material file.

The reference layout of the columns follows the general layout in [38], and shown in Figure 3a. To compute the slab thickness for the reference design we fix the column locations and optimize only the thickness, which equals to $h_{ref} = 0.331[m]$, with resultant concrete volume of $V_{ref} = 285.81\left[m^3\right]$.

In Figure 3b we present the relative deflections, where the deflections reach the allowed values only at the cantilever span at the bottom of the plan, while in broad areas of the floor the deflections are far form the allowed values, yielding $\bar{\delta}_{ref} = 0.331$. Re-optimization is not necessary because the design limit state requirements are met, as can be seen in Table 2, that summarise all the results.

After establishing the reference design, we add architectural path constraints to the optimization, where columns are allowed to move only along the partitioning walls. The partitioning walls are plotted in Figure 3a with thin lines, and are inspired by the layout of the partitioning walls in an architectural design of this floor, as can be found in San Francisco Planning Department's website [39], whereas the corresponding allowed paths are plotted in Figures 3b and 3c with white lines. The optimized design is presented in Figure 3c, where the slab thickness is $h_{arc} = 0.271\,[m]$ and the concrete volume is $V_{arc} = 234.17\,\left[m^3\right]$, which represents savings of 18.1%, relatively to the reference design. Thus, significant savings were possible while satisfying all architectural constraints. The second row of Table 2 summarises the results of the optimization with the path constraints.

Figure 3c also presents the relative deflections, where more regions of the floor reach their allowed deflection, and consequently the average relative deflection increases to $\bar{\delta}_{arc} = 0.427$. Keeping in mind that the bottom cantilever was the governing span at the reference design, we see that the optimization increases the length of the adjacent span, which reduced the deflections at the cantilever and enabled some thickness reduction. Another notable and somewhat less expected change in the design is the movement of the column at the vertical center-line of the floor (top of the plan) to the edge of the floor, increasing the length of the end span. This reduced the deflections at the neighboring spans from both sides and allowed for further reduction in the slab thickness.

So far we showed that significant savings are possible even when the design space is restricted to the portioning walls, as it would be in a sequential architectural-engineering design process. However, early collaboration between architects and engineers may increase the design freedom and facilitate further savings. To demonstrate the potential of a concurrent design process, we performed another

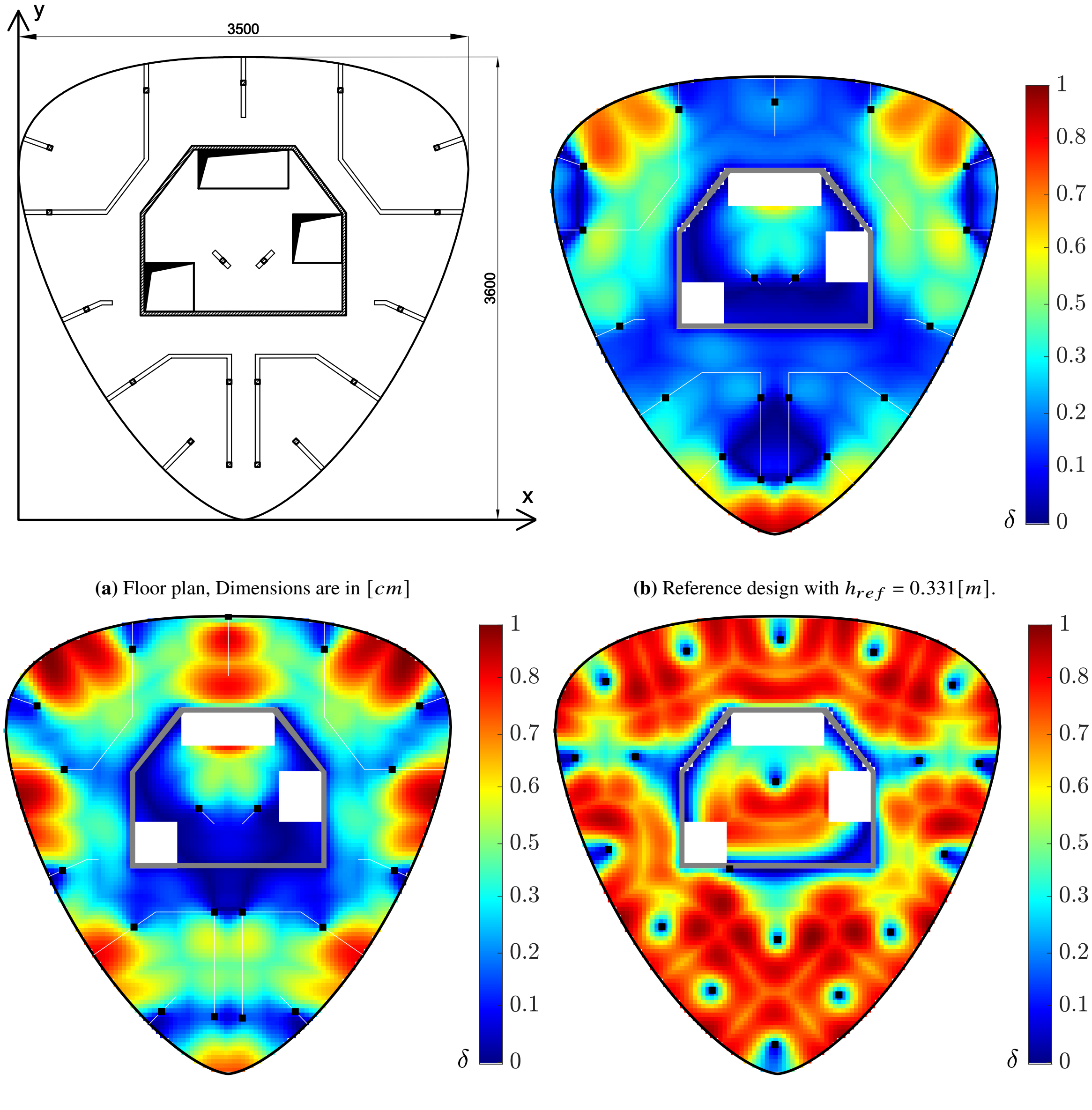

(a) Floor plan, Dimensions are in $[cm]$

(b) Reference design with $h_{ref} = 0.331[m]$.

(c) Optimized design with AC, $h_{arc} = 0.271[m](-18.1\%)$

(d) Free optimized design. $h = 0.1836[m](-44.5\%)$

Fig. 3. Reference and optimization results for the rounded triangular floor. At the reference design the deflections reach the allowed value only in one region of the floor, indicating sub-optimal design with $\bar{\delta}_{ref} = 0.331$. When optimized with architectural constraints, to ensure that the columns remain along the partitioning walls (marked with white lines), the deflection constraint becomes active in more spans with $\bar{\delta}_{arc} = 0.427$. At the free optimized design the deflections reach the allowed value in most span of the floor, thus indicating good utilization of the feasible space with $\bar{\delta}_{arc} = 0.659$. Surprisingly, one column merged with the core walls, thus practically eliminating this column.

optimization, this time without any limitation on the column layout. The optimized slab thickness is $h = 0.1836[m]$ and the resultant concrete volume is $V = 158.607\ [m^3]$, which represents volume saving of 44.5%. Figure 3d presents the relative deflection map and the optimized column layout,

	$h[m]$	$V\left[m^3\right]$	δ_{max}	$\bar{\delta}$	$\mu_{rx,max}$	$\mu_{rx,min}$	$\mu_{ry,max}$	$\mu_{ry,min}$	$\tau_{xz,max}$	$\tau_{yz,max}$
ref	0.331	285.81	1.0	0.331	0.252	-0.451	0.220	-0.320	0.492	0.528
opt. arc.	0.271	234.17 (-18.1%)	1.0	0.427	0.296	-0.574	0.260	-0.557	0.570	0.538
opt. free	0.184	158.61 (-44.5%)	1.0	0.659	0.415	-0.822	0.436	–0.793	0.681	0.672

Table 2. Results of the rounded triangular floor. top row: reference design, middle row: optimized design with architectural constraints, bottom row: free optimization. It can be see that in all cases the deflection constraint is the only active constraint, where the rate at which the feasible space is utilized increases with the design freedom.

which differs notably from the reference layout in Figure 3b. Surprisingly, one of the columns that was originally located inside the core has merged with the core wall. Thus, the column is not active and the optimization effectively converged to a solution with fewer columns. Looking at Figure 3d it is clear that the deflections across most of the floor approach the allowed deflection, and accordingly $\bar{\delta} = 0.659$. All other constraints are inactive, as can be seen at the third row of Table 2, and re-optimization was not needed.

In this example we included path constraints in the optimization and showed that even when the column are allowed to move only along the partitioning walls, thus having no 'architectural cost', significant savings are possible. Furthermore, we showed that when the optimization is granted with complete freedom, the concrete savings increases dramatically, but also the architectural cost increases. In the next example we explore further this trade off between the structural efficiency and the architectural cost.

4.3. Example 3: Irregular Residential Floor

In this section, we investigate the relation between the design freedom and the potential concrete savings. We approach this issue by examining the effect of the maximal allowed modification to the locations of columns, compared to a reference configuration – namely, a given architectural plan.

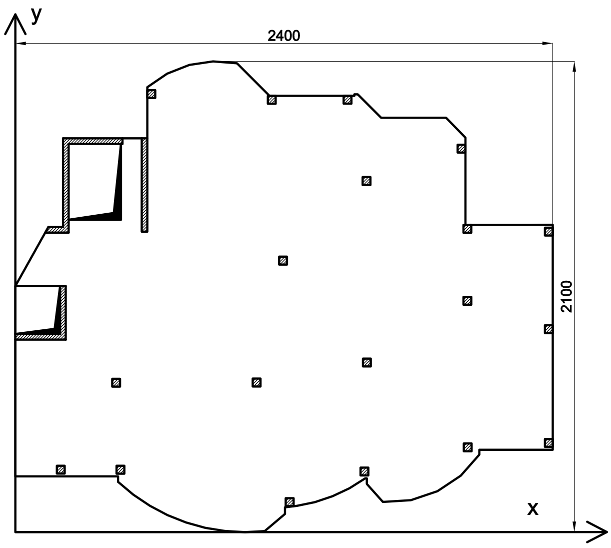

Fig. 4. Floor plan for example 3, including the reference layout of columns, dimensions are in $[cm]$.

Thus, we introduce an areal architectural constraint through an additional layer of parametrization:

$$x_i\,(t_i, s_i) = \Delta_{max} t_i + x_{i0}, \quad \text{and} \quad y_i\,(t_i, s_i) = \Delta_{max} s_i + y_{i0}, \quad \text{with} \quad -1 \le t_i, s_i \le 1,$$

where Δ_{max} is the maximal allowed change in a column location, and (x_{i0}, y_{i0}) are the column's coordinates in the reference design. Thus, each column is allowed to move only within a local box that is centered at the reference location of this column and has side lengths of $2\Delta_{max}$. Other shapes can be as easily parameterized to account for a variety of areal architectural constraints.

The selected floor plan in this example is inspired by a floor geometry that was presented by He et al. [40] in the context of yield line identification. This is an irregular floor in a residential building, supported by 19 square columns with side length of $0.35[m]$ and several walls, as can be seen in the floor plan in Figure 4. The thickness of the walls is $0.25[m]$, and accordingly the FE mesh consists of square elements with $0.2[m]$ side length. The applied forces and other parameters are the same as in the previous examples. All geometrical data, including the column locations, can be found in the Supplementary Material file.

In the following we will perform series of optimizations with increasing values of Δ_{max}, representing increasing levels of architectural freedom, and then investigate the trade-offs with the concrete savings. For convenience, all numerical results discussed herein are summarized at the end of this section in Table 3.

We begin with $\Delta_{max} = 0$, which is essentially optimizing the thickness of the slab while keeping the columns at their reference location. The resulting reference thickness is $h_{ref} = 0.2226[m]$ and the corresponding concrete volume is $V_{ref} = 82.15\ \left[m^3\right]$. The first row in Table 3 summarise the results of the reference design, where it is evident that the deflections constraint is the only active constraint, and re-optimization was not necessary.

Next, we set $\Delta_{max} = 0.1[m]$, allowing for very minor adjustment of the column locations, which probably has very little architectural cost. The optimized slab thickness is $h = 0.2109[m]$ which reflects a reduction of 5.3% in concrete volume with respect to the reference design. Again, the deflection constraint is the only active constraint and re-optimization is not necessary.

Increasing Δ_{max} further leads to greater concrete savings, as can be seen in Figure 5 that depicts the concrete volumes for different values of Δ_{max}. The right most point on the curve corresponds to $\Delta_{max} = \infty$ and represents the extreme case where the columns are free to move, where mathematically we omitted the architectural constraints for this optimization. The optimized slab thickness in this case is $h_\infty = 0.1126$, with concrete volume of $V_{opt} = 41.531\ \left[m^3\right]$, and not insignificant concrete savings of 49.4%.

Increasing the design freedom increases the extent at which the optimization utilizes the available feasible space. This is evident from Figure 5 that displays also the relative deflections for $\Delta_{max} = \{0, 0.5, 3, \infty\}\ [m]$ where $\bar{\delta}$ increases with the design freedom. Likewise, beginning at $\Delta_{max} = 1.1[m]$ and on, the moment constraint becomes also active. Thus, the moment and shear values initially exceed the desired threshold values, and re-optimization was necessary, after which all constraints are met and the objective function value increases (i.e., get worse). However, for $\Delta_{max} = 3.0[m]$ and $\Delta_{max} = \infty$ the re-optimized design results in slightly thinner slab than the corresponding optimized thicknesses when only deflection constraint was considered. Thus, indicating convergence to a local minima at the first optimization attempts, which is not unlikely in non-convex optimization. Nevertheless, in most

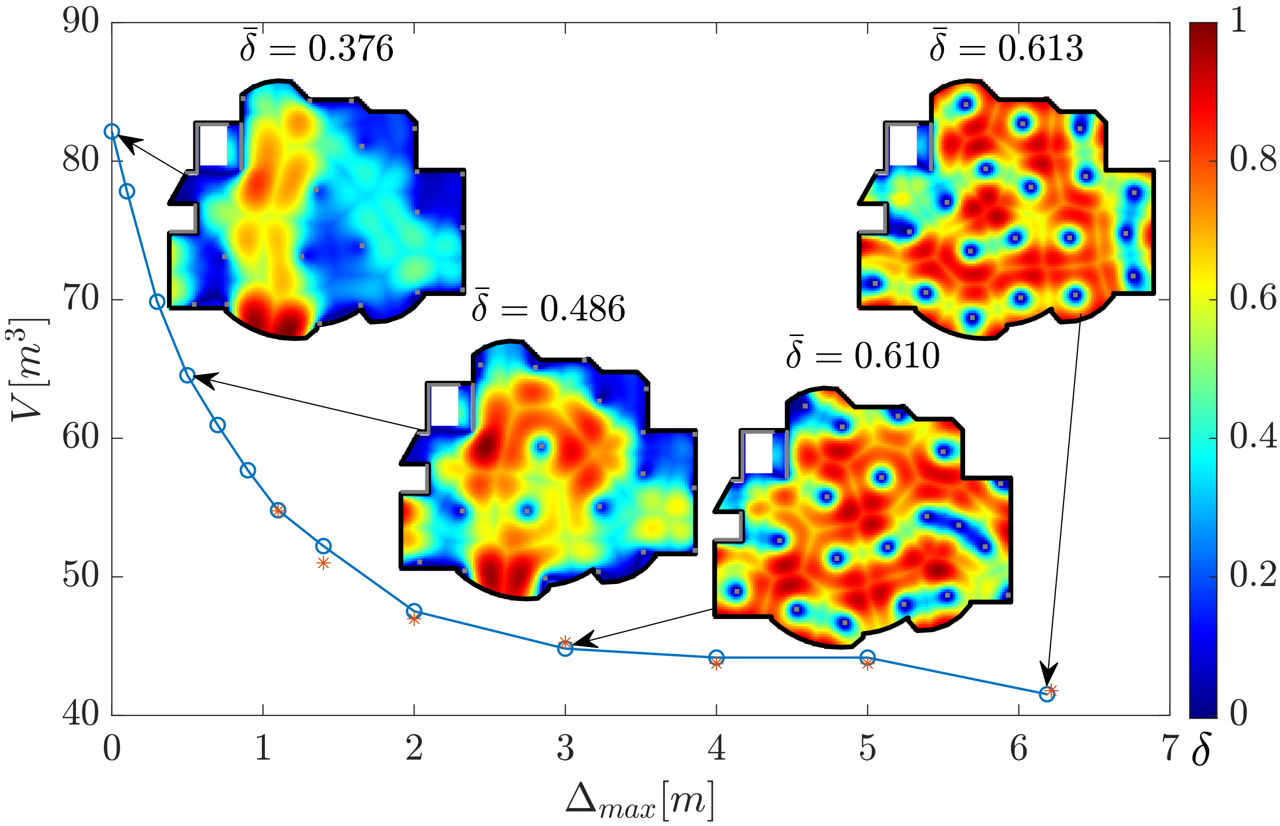

Fig. 5. Optimized concrete volume for different values of Δ_{max}. The steep slope at low values of Δ_{max} indicates that even a small update of the column layout can significantly affect the concrete volume. The red asterisks represent infeasible optimization results that were obtained with the deflection constraint only. Increasing the design freedom results in larger concrete savings that reach 49.4%. The color maps present the distribution of the relative deflection, δ, for $\Delta_{max} = \{0, 0.5, 3.0, \infty\}\,[m]$. It is evident that increasing Δ_{max} results in more efficient design with higher $\bar{\delta}$.

cases adding more constraints leads to higher (worse) objective function values, as apparent from the results in Table 3 and in Figure 5. Therein, the optimization trials that were re-optimized are marked with an asterisk.

Another interesting observation from the the relative deflection plots in Figure 5 is that as the design freedom increases, the columns distribution tend be more uniform, with small differences between bay lengths. The reason for this is that large differences in adjacent bay lengths result in non-zero slope of the deflection surface, and therefore are generally not optimal [37, 28]. Thus, we expect optimized column layouts to be characterised with relatively uniform distribution, which can be used to set a good initial design. Interestingly, since the effect of pattern loading reduces with the difference between bay lengths, including pattern loading in the formulation could result in larger savings in concrete volume. Therefore, the obtained savings are possibly somewhat on the conservative side.

Additionally, we note that the optimizations with $\Delta_{max} = 4.0[m]$ and $\Delta_{max} = 5.0[m]$ converged to the same optimum. A possible explanation for this is the non-convexity of the optimization problem. Thus, the optimal solution might have a discrete dependence on the design space freedom. This could also explain why the optimal concrete volume that corresponds to $\Delta_{max} = \infty$ is lower than one would expect based on the graph in Figure 5.

Finally, since Δ_{max} can be regarded as a measure of the architectural cost, the curve in Figure 5 can be interpreted as the trade-off between the architectural cost and the concrete volume. This trade-off curve is convex and therefore small increase in the architectural cost with respect to a traditionally obtained reference design, may lead to significant reduction in concrete volume. For example, allowing $\Delta_{max} = 0.9[m]$ results in almost 30% reduction.

5. Discussion and conclusions

We presented a method to minimize the concrete consumption in slabs by optimizing the column locations, and then use it to investigate the sensitivity of the thickness to the column locations. We formulate a deflection constraint that is differentiable with respect to the changing columns locations, as well as moment and shear constraints, and include architectural constraints through the explicit design parametrization. For any given floor plan, the method generates an optimized layout of columns and the corresponding minimal required slab thickness. We use gradient-based optimization with analytically derived sensitivities, which results in a very effective numerical method that can be used for problems with a large number of design variables, that would have not been practical with zero-order optimization methods. For example, simultaneous optimization of a large number of columns within an extended framework that includes also the column dimensions and a slab with varying thickness.

Through three different examples we show the ability of the proposed method to cope with any floor geometry, any number of columns and a range of architectural-geometrical constraints. The

Table 3. Optimization of the irregular slab with increasing level of design freedom. * Indicates infeasible result obtained with deflection constraint only.

Δ_{max}	$h[m]$	$V\,[m^3]$		δ_{max}	$\bar{\delta}$	$\mu_{rx,max}$	$\mu_{rx,min}$	$\mu_{ry,max}$	$\mu_{ry,min}$	$\tau_{xz,max}$	$\tau_{yz,max}$
0(ref)	0.223	82.146	-	1.000	0.376	0.380	-0.680	0.225	-0.703	0.530	0.753
0.1	0.211	77.829	5.3%	1.000	0.397	0.388	-0.694	0.238	-0.757	0.534	0.721
0.3	0.189	69.856	15.0%	1.000	0.453	0.408	-0.784	0.279	-0.853	0.524	0.680
0.5	0.175	64.546	21.4%	1.000	0.486	0.394	-0.834	0.338	-0.892	0.494	0.694
0.7	0.165	60.958	25.8%	1.000	0.516	0.382	-0.838	0.374	-0.919	0.473	0.805
0.9	0.156	57.693	29.8%	1.000	0.511	0.400	-0.863	0.391	-0.949	0.536	0.946
1.1*	0.148	54.765	33.3%	1.000	0.530	0.412	-0.903	0.402	-1.070	0.675	1.092
1.1	0.149	54.808	33.3%	1.000	0.524	0.412	-0.901	0.399	-0.999	0.679	0.997
1.4*	0.138	51.007	37.9%	1.000	0.548	0.468	-1.046	0.424	-1.170	0.874	1.116
1.4	0.142	52.219	36.4%	0.998	0.542	0.556	-0.937	0.420	-1.000	0.637	0.850
2.0*	0.127	46.976	42.8%	0.999	0.575	0.497	-1.215	0.466	-1.145	1.134	0.931
2.0	0.129	47.524	42.1%	0.998	0.552	0.502	-0.952	0.463	-1.000	0.776	0.781
3.0*	0.123	45.269	44.9%	1.000	0.601	0.516	-1.019	0.547	-1.095	0.556	0.794
3.0	0.121	44.820	45.4%	1.001	0.610	0.592	-0.949	0.544	-1.000	0.554	0.826
4.0*	0.119	43.745	46.7%	0.996	0.622	0.591	-1.040	0.510	-1.114	0.582	0.744
4.0	0.120	44.174	46.2%	0.996	0.596	0.608	-0.926	0.481	-0.999	0.572	0.676
5.0*	0.119	43.745	46.7%	0.996	0.622	0.591	-1.040	0.510	-1.114	0.582	0.744
5.0	0.120	44.174	46.2%	0.996	0.596	0.608	-0.926	0.481	-0.999	0.572	0.676
6.0*	0.119	43.745	46.7%	0.996	0.622	0.591	-1.040	0.510	-1.114	0.582	0.744
6.0	0.120	44.174	46.2%	0.996	0.596	0.608	-0.926	0.481	-0.999	0.572	0.676
∞*	0.113	41.793	49.1%	1.000	0.638	0.587	-1.149	0.528	-1.342	0.694	1.029
∞	0.113	41.531	49.4%	1.000	0.613	0.521	-0.947	0.501	-1.001	0.576	0.774

results show that even when the columns are allowed to move only along the partitioning walls, notable savings of up to 18% are possible. Furthermore, we show that increasing the granted freedom to the optimization dramatically increases the potential for concrete savings, which may reach as high as 50%. Interestingly, even minor changes in column locations (in the order of $0.1[m] - 0.9[m]$) with respect to a traditional design, may result in substantial savings of 5% − 30%.

The results of this study indicate that the optimal column layout is not trivial and that traditional designs are often sub-optimal. Thus, given the high sensitivity of the slab thickness to the columns locations, the proposed method can be used to fine-tune column layouts to reduce the slab thickness in many buildings. Furthermore, collaborative architectural and structural design from the preliminary stages when the architectural layout and consequently the column layout are determined, is key to achieve significant concrete savings.

Another interesting observation that can be made is the direct relation between the optimality of the column layout and the rate at which the deflection constraint is satisfied. Thus, the mean relative deflection can be used as an indicator for the effectiveness of a design, with an estimated theoretical maximum value in the range $\bar{\delta}_{max} \in [0.64, 0.77]$.

Throughout this research the architectural requirements were imposed as hard constraints based on existing architectural designs. However, explicit and quantitative consideration of the architectural cost is an interesting direction for future research, which will allow to construct more meaningful Pareto fronts that illustrate the trade-offs between structural efficiency and architectural performance. Additionally, although a substantial reduction in concrete volume is possible by the proposed method, it is possible that more steel reinforcement will be needed. Thus, the optimal balance between concrete and steel in terms of cost and environmental impact still remains open for future work. Furthermore, including also non-linear material response and plasticity might reveal interesting failure modes.

6. Data Availability Statement

Some or all data, models, or code that support the findings of this study are available from the corresponding author upon reasonable request.

7. Acknowledgments

This research was funded by the Ministry of Construction and Housing, Israel. The financial support is gratefully acknowledged.

8. Conflict of Interest

The authors declare that they have no conflict of interest.

Appendix A. Sensitivity analysis

Since we implement gradient based optimization, the first-order derivatives should be provided. In this section we present in detail all calculations involved in the computation of these derivatives. We note that the analytical sensitivities were verified by comparing to numerical derivatives obtained with finite differences method and were found to be accurate.

The derivatives with respect to the mathematical design variables are obtained by the chain rule

$$\frac{\partial f_\alpha}{\partial \mathbf{X}} = \frac{\partial f_\alpha}{\partial \tilde{\mathbf{X}}} \frac{\partial \tilde{\mathbf{X}}}{\partial \mathbf{X}}, \quad \text{with} \quad \alpha \in \{0, 1, 2, 3\}, \tag{A.1}$$

where $\frac{\partial \tilde{\mathbf{X}}}{\partial \mathbf{X}} = \mathbf{N}^{-1}$ is the Jacobian matrix, and $\frac{\partial f_\alpha}{\partial \tilde{\mathbf{x}}}$ are the derivatives of the α functional with respect the physical design variables and discussed in following sub-sections.

Appendix A.1. Volume Objective function

The sensitivities of the volume can be obtained explicitly because it does not depend on the structural response. Thus, we differentiate Eq. (12)

$$\frac{\partial V}{\partial \tilde{X}} = \sum_{\ell=1}^{N_\ell} \frac{\partial h_\ell}{\partial \tilde{X}} A_\ell, \tag{A.2}$$

where $\tilde{X}$ is any of the physical design variables. The derivative of the elemental thickness h_ℓ with respect the slab thickness is simply $\frac{\partial h_\ell}{\partial h} = 1.0$ and zero with respect the columns locations.

Appendix A.2. Deflection Constraint

In the perspective of the individual MMA iteration, the threshold value of the constraint is constant. Therefore the derivative of the deflection constraint equals to the derivative of the maximal relative deflection, scaled by $1/\tilde{\delta}^*$

$$\frac{\partial f_1}{\partial \tilde{X}} = \frac{1}{\tilde{\delta}^*}\frac{\partial \tilde{\delta}}{\partial \tilde{X}}. \tag{A.3}$$

Thus, we focus on the derivative of $\tilde{\delta}$.

The deflection constraint is an implicit function of the design variables and therefore we adopt the adjoint approach. The basic idea is to augment the functional with the equilibrium residual multiplied by an adjoint vector that will be selected such that the implicit terms will vanish. Thus, the augmented functional is

$$\tilde{\delta}_a = \tilde{\delta} - \boldsymbol{\lambda}_\delta^T \left(\mathbf{K}\mathbf{u}_s - \mathbf{f}_s\right). \tag{A.4}$$

Since the equilibrium residual equals to zero, the augmented functional equals to the original functional and so are the derivatives.

Thus, we differentiate the augmented constraint with respect to the design variables. Keeping in mind that the deflection constraint also depends explicitly on the design variables through the allowed deflection, we get

$$\frac{\partial \tilde{\delta}_a}{\partial \tilde{X}} = \frac{\partial \tilde{\delta}}{\partial \mathbf{u}_s}\frac{\partial \mathbf{u}_s}{\partial \tilde{X}} + \frac{\partial \tilde{\delta}}{\partial \mathbf{w}_A}\frac{\partial \mathbf{w}_A}{\partial \tilde{X}} - \boldsymbol{\lambda}_\delta^T \left(\frac{\partial \mathbf{K}}{\partial \tilde{X}}\mathbf{u}_s + \mathbf{K}\frac{\partial \mathbf{u}_s}{\partial \tilde{X}} - \frac{\partial \mathbf{f}_s}{\partial \tilde{X}}\right). \tag{A.5}$$

Since the derivatives of the augmented and original functionals are the same, we switch back to the original functional. As mentioned, the adjoint vector is computed such that the terms $\frac{\partial \mathbf{u}}{\partial \tilde{X}}$ will cancel each other. Thus, the derivative of the deflection is

$$\frac{\partial \tilde{\delta}}{\partial \tilde{X}} = \frac{\partial \tilde{\delta}}{\partial \mathbf{w}_A}\frac{\partial \mathbf{w}_A}{\partial \tilde{X}} - \boldsymbol{\lambda}_\delta^T \left(\frac{\partial \mathbf{K}}{\partial \tilde{X}}\mathbf{u}_s - \frac{\partial \mathbf{f}_s}{\partial \tilde{X}}\right) \quad \text{with} \quad \mathbf{K}^T\boldsymbol{\lambda}_\delta = \left(\frac{\partial \tilde{\delta}}{\partial \mathbf{u}_s}\right)^T \tag{A.6}$$

The adjoint vector $\boldsymbol{\lambda}_\delta$ and $\frac{\partial \tilde{\delta}}{\partial \hat{\mathbf{u}}_s}$ are the same as presented in [41]. The derivative of the maximal approximated relative deflection with respect to the allowed deflection is obtained by substituting Eq. (13) into Eq. (14) and differentiating

$$\frac{\partial \tilde{\delta}}{\partial \mathbf{w}_A} = -\tilde{\delta} \left[\sum_j \delta_j^p \right]^{-1} \sum_j \delta_j^{p-1} w_j \left(w_A \right)_j^{-2}. \tag{A.7}$$

The derivative of the allowed deflections with respect to the design variables is obtained by replacing $r_{min,j}$ in Eq. (17) with its derivative, and multiplying by $\frac{1}{750}$ according to Eq. (16). Thus, by differentiating Eq. (18) we obtain the derivative of the distance form the j^{th} node to the closest column,

$$\frac{\partial r_{min,j}}{\partial \tilde{X}} = r_{min,j} \sum_i r_{ij}^{p-1} \frac{\partial r_{ij}}{\partial \tilde{X}}. \tag{A.8}$$

The derivative $\frac{\partial r_{ij}}{\partial \tilde{X}}$ is computed by differentiating the distance between the i^{th} column and the j^{th} node, where for all design variables other than the i^{th} column location, the derivative is equal to zero.

The next term in Eq. (A.6) is the derivative of the stiffness matrix with respect to the design variables, which were discussed in [28] and are brought here for completeness.

As mentioned, the stiffness matrix of the supported plate is simply summation of the plate's stiffness matrix and the equivalent matrices of the columns

$$\mathbf{K} = \mathbf{K}_p + \sum_{i=1}^{N_{col}} \mathbf{K}_{cp,i}. \tag{A.9}$$

Thus, the derivatives with respect the column locations affect only the added equivalent column stiffness matrices. Thus, by differentiating Eq. A.9 with respect the x coordinate of the i^{th} column we get

$$\frac{\partial \mathbf{K}}{\partial x_{c,i}} = \frac{\partial \mathbf{K}_{cp,i}}{\partial x_{c,i}}. \tag{A.10}$$

The derivative of equivalent stiffness matrix of the i^{th} column with respect $x_{c,i}$ is obtained by differentiating Eq. (1)

$$\frac{\partial \mathbf{K}_{cp,i}}{\partial x_{c,i}} = \sum_j^{N_n} \left[\frac{\partial \mathbf{K}_{cp,i}}{\partial x_{c,i}} \right]_j = \sum_j^{N_n} \frac{\partial w_{ij}}{\partial x_{c,i}} \mathbf{K}_{c,i}. \tag{A.11}$$

The summation sign stands for assembly according the nodal DOF. The derivative of the projection weight is obtained by differentiating Eq. (2) and substituting into Eq. (3),

$$\frac{\partial w_{ij}}{\partial x_{c,i}} = \frac{\frac{\partial \tilde{w}_{ij}}{\partial x_{c,i}} \sum_k \tilde{w}_{ik} - \tilde{w}_{ij} \sum_k \frac{\partial \tilde{w}_{ik}}{\partial x_{c,i}}}{\left(\sum_k \tilde{w}_{ik}\right)^2} \tag{A.12}$$

with

$$\frac{\partial \tilde{w}_{ij}}{\partial x_{c,i}} = -\frac{\beta}{\eta}\left(\frac{r_{ij}}{\eta}\right)^{2\beta-1} \frac{\partial r_{ij}}{\partial x_{c,i}} \tilde{w}_{ij}. \tag{A.13}$$

The derivatives with respect to $y_{c,i}$ are computed in the same way.

The derivative of the stiffness matrix with respect the thickness design variable affect the plate's stiffness matrix, $\mathbf{K}_p$, and are obtained by differentiating the elemental stiffness matrices and thereafter assembling in a regular manner. The plate's stiffness matrix is assembled in a standard manner, for a mesh with identical elements

$$\mathbf{K}_p = \sum_{\ell} \mathbf{K}_{\ell} = \sum_{\ell} \mathbf{B}_{\ell}^T \mathbf{D}_{\ell} \mathbf{B}_{\ell} = \sum_{\ell} \mathbf{B}^T \mathbf{D} \mathbf{B}, \tag{A.14}$$

where $\mathbf{B}$ and $\mathbf{D}$ are the elemental generalized differentiation and constitutive matrices. Thus, after differentiating we get

$$\frac{\partial \mathbf{K}_p}{\partial h} = \sum_{\ell} \mathbf{B}^T \frac{\partial \mathbf{D}}{\partial h} \mathbf{B}, \tag{A.15}$$

where the derivative of the constitutive matrix is computed by explicit differentiation.

The final term in Eq. (A.6) is the derivative of the external forces vector with respect to the design variables. The external forces depend on the design through the thickness and the concrete mass density

$$\frac{\partial \mathbf{f}_s}{\partial h} = \sum_{\ell} \frac{\gamma_c A_{\ell}}{4}, \tag{A.16}$$

where γ_c is the mass density of the concrete, A_{ℓ} is the area of the elements, and the summation sign stands for assembly according the elemental DOF.

Appendix A.3. Shear Constraint

Similarly to the deflection constraint, the derivative of the shear constraint is,

$$\frac{\partial f_2}{\partial \tilde{X}} = \frac{1}{\tilde{\sigma}_{ts}^*} \frac{\partial \tilde{\sigma}_{ts}}{\partial \tilde{X}}. \tag{A.17}$$

Since $\tilde{\sigma}_{ts}$ is an implicit function of the design variables, we use the adjoint approach again. The augmented functional is

$$(\tilde{\sigma}_{ts})_a = \tilde{\sigma}_{ts} - \boldsymbol{\lambda}_\tau^T (\mathbf{K}\mathbf{u}_d - \mathbf{f}_d). \tag{A.18}$$

This time, there is no explicit dependence and therefore after differentiating and replacing the augmented functional with the original one, we get

$$\frac{\partial \tilde{\sigma}_{ts}}{\partial \tilde{X}} = \frac{\partial \tilde{\sigma}_{ts}}{\partial \mathbf{u}_d}\frac{\partial \mathbf{u}_d}{\partial \tilde{X}} - \boldsymbol{\lambda}_\tau^T \left(\frac{\partial \mathbf{K}}{\partial \tilde{X}}\mathbf{u}_d + \mathbf{K}\frac{\partial \mathbf{u}_d}{\partial \tilde{X}} - \frac{\partial \mathbf{f}_d}{\partial \tilde{X}}\right). \tag{A.19}$$

Selecting the adjoint vector such that the terms involving $\frac{\partial \mathbf{u}_d}{\partial \tilde{X}}$ will vanish, we get

$$\frac{\partial \tilde{\sigma}_{ts}}{\partial \tilde{X}} = -\boldsymbol{\lambda}_\tau^T \left(\frac{\partial \mathbf{K}}{\partial \tilde{X}}\mathbf{u}_d - \frac{\partial \mathbf{f}_d}{\partial \tilde{X}}\right) \quad \text{with} \quad \mathbf{K}^T \boldsymbol{\lambda}_\tau = \left(\frac{\partial \tilde{\sigma}_{ts}}{\partial \mathbf{u}_d}\right)^T. \tag{A.20}$$

The only term that is unknown is $\frac{\partial \tilde{\sigma}_{ts}}{\partial \hat{\mathbf{u}}_d}$ which is obtained by differentiation of Eq. (20)

$$\frac{\partial \tilde{\sigma}_{ts}}{\partial \mathbf{u}_d} = \hat{\tilde{\sigma}}_{ts} \left(\sum_{j=1}^{2N_{nodes}} \sigma_{ts,j}^p\right)^{-1} \left(\boldsymbol{\sigma}_{ts}^{\circ(p-1)}\right)^T \frac{\partial \boldsymbol{\sigma}_{ts}}{\partial \mathbf{u}_d}, \tag{A.21}$$

where $\frac{\partial \boldsymbol{\sigma}_{ts}}{\partial \mathbf{u}_d}$ is obtained by differentiating (5), multiplying with $\mathbf{W}$, and selecting the appropriate terms

$$\frac{\partial \mathbf{S}}{\partial \mathbf{u}_d} = \mathbf{W}^T \mathbf{D}\mathbf{B} \tag{A.22}$$

Appendix A.4. Moment Constraint

The derivative of the moment constraint is

$$\frac{\partial f_3}{\partial \tilde{X}} = \frac{1}{\tilde{\mu}^*}\frac{\partial \tilde{\mu}}{\partial \tilde{X}} \tag{A.23}$$

The augmented moment functional is

$$(\tilde{\mu})_a = \tilde{\mu} - \boldsymbol{\lambda}_\mu^T (\mathbf{K}\mathbf{u}_d - \mathbf{f}_d). \tag{A.24}$$

The relative moment is related to the design variables both implicitly and explicitly, $\tilde{\mu} = \tilde{\mu}\left(\tilde{X}, \mathbf{u}_d\left(\tilde{X}\right)\right)$. Therefore, we distinguish between the total derivative and the partial derivative of the relative moment by using different operators notations of d and ∂, respectively. Thus, after differentiating the above equation and getting back to the original moment functional we get

$$\frac{d\tilde{\mu}}{d\tilde{X}} = \frac{\partial\tilde{\mu}}{\partial\mathbf{u}_d}\frac{\partial\mathbf{u}_d}{\partial\tilde{X}} + \frac{\partial\tilde{\mu}}{\partial\tilde{X}} - \boldsymbol{\lambda}_\mu^T\left(\frac{\partial\mathbf{K}}{\partial\tilde{X}}\mathbf{u}_d + \mathbf{K}\frac{\partial\mathbf{u}_d}{\partial\tilde{X}} - \frac{\partial\mathbf{f}_d}{\partial\tilde{X}}\right). \tag{A.25}$$

After eliminating the derivatives $\frac{\partial\mathbf{u}}{\partial\tilde{X}}$ by finding a proper adjoint vector, the derivative of the moment constraint is

$$\frac{d\tilde{\mu}}{d\tilde{X}} = \frac{\partial\tilde{\mu}}{\partial\tilde{X}} - \boldsymbol{\lambda}_\mu^T\left(\frac{\partial\mathbf{K}}{\partial\tilde{X}}\mathbf{u}_d - \frac{\partial\mathbf{f}_d}{\partial\tilde{X}}\right) \quad \text{with} \quad \mathbf{K}^T\boldsymbol{\lambda}_\mu = \left(\frac{\partial\tilde{\mu}}{\partial\mathbf{u}_d}\right)^T. \tag{A.26}$$

The explicit derivative can be written in the following form

$$\frac{\partial\tilde{\mu}}{\partial\tilde{X}} = \frac{\partial\tilde{\mu}}{\partial h}\frac{\partial h}{\partial\tilde{X}}, \quad \text{with} \quad \frac{\partial\tilde{\mu}}{\partial h} = \tilde{\mu}\left(\sum\boldsymbol{\mu}^p\right)^{-1}\left(\frac{\partial\boldsymbol{\mu}}{\partial h}\right)^T\boldsymbol{\mu}^{\circ(p-1)}, \tag{A.27}$$

where $\circ$ indicates elementwise operation. The derivative of the relative W&A moments with respect the slab thickness is given by

$$\frac{\partial\boldsymbol{\mu}}{\partial h} = \left\{\left[\left(\frac{\partial\mathbf{M}}{\partial h}\right)^T\mathbf{M}_c - \mathbf{M}^T\frac{\partial\mathbf{M}_c}{\partial h}\right]\circ\mathbf{M}_c^{\circ-2}\right\}. \tag{A.28}$$

In the equation above, $\mathbf{M}$ is a vector with all W&A moments at all nodes and $\mathbf{M}_c$ is a vector with the moment capacities. All W&A moments have similar structure, thus for example the derivative of $M_{rx,max}$ is given by

$$\frac{\partial M_{rx,max}}{\partial h} = \frac{\partial M_{xx}}{\partial h} + \operatorname{sign}\left(M_{xy}\right)\frac{\partial M_{xy}}{\partial h}. \tag{A.29}$$

The derivatives of the plate moments are obtained by differentiating Eq. (5), multiplying with $\mathbf{W}$, and selecting the moments components

$$\frac{\partial\mathbf{S}}{\partial h} = \mathbf{W}^T\frac{\partial\mathbf{D}}{\partial h}\mathbf{B}\hat{\mathbf{u}}_d. \tag{A.30}$$

The derivative of the moment capacities is obtained by differentiating Eq. (23), where the only derivative with non zero value is the derivative with respect the slab thickness

$$\frac{\partial\mathbf{M}_c}{\partial h} = \mathbf{1}\left(h - d_s\right)0.64 f_{cd}. \tag{A.31}$$

The last component is the derivative of the approximate maximum relative moment with respect to the displacements which is obtained by differentiating Eq. (25)

$$\frac{\partial \tilde{\mu}}{\partial \mathbf{u}_d} = \tilde{\mu} \left(\sum \boldsymbol{\mu}^p\right)^{-1} \left(\frac{\partial \mathbf{M}}{\partial \mathbf{u}_d}\right)^T \left\langle \mathbf{M}_c^{\circ -1} \right\rangle \boldsymbol{\mu}^{\circ (p-1)} \tag{A.32}$$

where $< \cdot >$ is a diagonal operator and the derivatives of the nodal moments were computed in Eq. (A.22). All other components are given in previous derivations of the SA of the other functionals.

Appendix B. Implementation

We solve the optimization problem using a gradient based algorithm due to its efficiency in dealing with large number of design variables. Specifically, the MMA algorithm [36] which is common algorithm in structural optimization. However, a successful optimization requires also several implementational techniques which are described in the following sub-sections together with some related considerations. Thereafter, we summarise all the geometrical data that is used in the examples that are presented in this study.

Appendix B.1. Convergence Criteria

The basic convergence criterion is related to the change in the objective function. Because the objective function might have noisy behavior, we consider the average change in the objective function over the previous N_{f0} iteration. We define a cumulative convergence parameter f_{0c} that is promoted each iteration that the change in average objective function is less than f_{0c}^* and demoted otherwise. The objective function is converged when the cumulative convergence parameter is equal to f_{0ci}. Additionally, we require that at convergence the solution is feasible, such that the maximum of all constraints is less than $f^* = 0.01$

Appendix B.2. Dynamic Move Limits

It was observed that the optimization may have oscillatory behavior of the design variables, and as a result the objective function, do not converge. Therefore we implement a dynamic move limit mechanism such that the move limit of an oscillating design variable is tightened and the move limit of monotonically behaving design variables gets wider. Thus, each design variable has a stability index SI that is promoted each time that the change in design variable value is the same as in the previous iteration and demoted otherwise. The stability index of the m^{th} design variable at the the n^{th} iteration is given by

$$SI_m^n = SI_m^{n-1} + \operatorname{sign}\left[\left(X_m^n - X_m^{n-1}\right)\left(X_m^{n-1} - X_m^{n-2}\right)\right]. \tag{B.1}$$

Once the stability index of a design variable reaches the positive or negative threshold values, SI^+ and SI^-, the move limit is updated accordingly as follows

$$ML_m^n = \begin{cases} ML_m^{n-1}\alpha & SI_m^n = SI^+ \\ ML_m^{n-1}\alpha^{\left(-\frac{SI^+}{SI^-}\right)} & SI_m^n = SI^- \\ ML_m^{n-1} & \text{otherwise} \end{cases}, \quad \text{with} \quad \alpha > 1. \tag{B.2}$$

Additionally, it was observed that the oscillations may occur on a larger scale, where the design variables behave monotonically with respect the neighboring iterations but the optimization fail to converge. In order to deal with this problem we monitor the number of times that the objection function crosses the average objective function at a predefined sampling widow of iterations. Thus, we define a threshold value for the number of intersections between the average and non-average objective functions, beyond which all move limits of all design variables are narrowed down. Herein we consider two sampling windows, representing two different scales of iterations, of 10 and 100 iterations and set the threshold value of intersections to 3 and 10 respectively. Thus, each time that any of the threshold values is reached, all move limits narrowed down by factor of 0.9. Finally, we set minimum and maximum values for the move limits of 1×10^{-2} and 1×10^{-4}, respectively.

Appendix B.3. Numerical Damping And Continuation Of The Projection Radius

It was shown in [28] that the numerical performance of optimization of supports location can be significantly improved by implementing three techniques presenter therein. Namely: Control of initial design, continuation of the projection radii and numerical damping of the derivatives. In this study we implemented the numerical damping and the three stage continuation scheme of the projection radii as presented in [28]. The initial design control has not been implemented directly, since the initial designs herein are obtained manually and comply with the conditions of the initial control as defined in [28].

References

[1] R. M. Andrew, Global co 2 emissions from cement production, Earth System Science Data 10 (2018) pp.195–217. doi:https://doi.org/10.5194/essd-10-195-2018.

[2] C. Thirion, Putting the material in the right place: Investigations into the sustainable use of structural materials to reduce the initial embodied environmental impact of building structures, Ph.D. thesis, UCL (University College London), 2013. URL: https://discovery.ucl.ac.uk/id/eprint/1396779.

[3] W. Shanks, C. Dunant, M. P. Drewniok, R. Lupton, A. Serrenho, J. M. Allwood, How much cement can we do without? lessons from cement material flows in the uk, Resources, Conservation and Recycling 141 (2019) pp.441–454. doi:https://doi.org/10.1016/j.resconrec.2018.11.002.

[4] S. Weidner, A. Mrzigod, R. Bechmann, W. Sobek, Graue emissionen im bauwesen–bestandsaufnahme und optimierungsstrategien, Beton-und Stahlbetonbau 116 (2021) 969–977. doi:https://doi.org/10.1002/best.202100065.

[5] O. Sigmund, K. Maute, Topology optimization approaches, Structural and Multidisciplinary Optimization 48 (2013) 1031–1055. doi:10.1007/s00158-013-0978-6.

[6] J.-H. Zhu, W.-H. Zhang, L. Xia, Topology optimization in aircraft and aerospace structures

design, Archives of Computational Methods in Engineering 23 (2016) 595–622. doi:10.1007/s11831-015-9151-2.

[7] T. Dbouk, A review about the engineering design of optimal heat transfer systems using topology optimization, Applied Thermal Engineering 112 (2017) 841–854. doi:https://doi.org/10.1016/j.applthermaleng.2016.10.134.

[8] D. Yeo, R. D. Gabbai, Sustainable design of reinforced concrete structures through embodied energy optimization, Energy and buildings 43 (2011) 2028–2033. doi:https://doi.org/10.1016/j.enbuild.2011.04.014.

[9] D. Yeo, F. A. Potra, Sustainable design of reinforced concrete structures through co 2 emission optimization, Journal of structural engineering 141 (2015) B4014002. doi:https://doi.org/10.1061/(ASCE)ST.1943-541X.0000888.

[10] H. Varaee, B. Ahmadi-Nedushan, Minimum cost design of concrete slabs using particle swarm optimization with time varying acceleration coefficients, World Appl Sci J 13 (2011) 2484–94.

[11] M. Aldwaik, H. Adeli, Cost optimization of reinforced concrete flat slabs of arbitrary configuration in irregular highrise building structures, Structural and Multidisciplinary Optimization 54 (2016) 151–164. doi:10.1007/s00158-016-1483-5.

[12] S. O. A. Olawale, O. P. Akintunde, M. O. Afolabi, M. A. Tijani, Design optimization of reinforced concrete waffle slab using genetic algorithm, Journal of Soft Computing in Civil Engineering 4 (2020) 46–62. doi:10.22115/SCCE.2020.224460.1195.

[13] M. A. Ismail, C. T. Mueller, Minimizing embodied energy of reinforced concrete floor systems in developing countries through shape optimization, Engineering Structures 246 (2021) 112955. doi:https://doi.org/10.1016/j.engstruct.2021.112955.

[14] M. Rady, S. Y. Mahfouz, S. E.-D. F. Taher, Optimal design of reinforced concrete materials in construction, Materials 15 (2022) 2625. doi:https://doi.org/10.3390/ma15072625.

[15] S. Eleftheriadis, P. Duffour, D. Mumovic, Bim-embedded life cycle carbon assessment of rc buildings using optimised structural design alternatives, Energy and Buildings 173 (2018) 587–600. doi:https://doi.org/10.1016/j.enbuild.2018.05.042.

[16] P. Foraboschi, M. Mercanzin, D. Trabucco, Sustainable structural design of tall buildings based on embodied energy, Energy and Buildings 68 (2014) pp.254–269. doi:https://doi.org/10.1016/j.enbuild.2013.09.003.

[17] M. Sahab, A. Ashour, V. Toropov, Cost optimisation of reinforced concrete flat slab buildings, Engineering structures 27 (2005) 313–322. doi:https://doi.org/10.1016/j.engstruct.2004.10.002.

[18] D. Shaw, J. Miles, A. Gray, Determining the structural layout of orthogonal framed buildings, Computers & Structures 86 (2008) pp.1856–1864. doi:https://doi.org/10.1016/j.compstruc.2008.04.009.

[19] P. Sharafi, L. H. Teh, M. N. Hadi, Conceptual design optimization of rectilinear building frames: A knapsack problem approach, Engineering Optimization 47 (2015) pp.1303–1323. doi:https://doi.org/10.1080/0305215X.2014.963068.

[20] A. Chepurnenko, E. Efimenko, D. Mailyan, B. Yazyev, The location of supports under the monolithic reinforced concrete slabs optimization, Magazine of Civil Engineering (2021) 10404. doi:10.34910/MCE.104.4.

[21] O. Sigmund, On the usefulness of non-gradient approaches in topology optimization, Structural and Multidisciplinary Optimization 43 (2011) 589–596. doi:10.1007/s00158-011-0638-7.

[22] J. H. Son, B. M. Kwak, Optimization of boundary conditions for maximum fundamental frequency of vibrating structures, American Institute of Aeronautics and Astronautics Journal 31 (1993) pp.2351–2357. doi:https://arc.aiaa.org/doi/pdf/10.2514/3.11935.

[23] R. Menassa, W. DeVries, Optimization methods applied to selecting support positions in fixture design, ASME Journal for Engineering for Industry 113 (1991) pp.412–418. doi:https://doi.org/10.1115/1.2899715.

[24] T. Buhl, Simultaneous topology optimization of structure and supports, Structural and Multidisciplinary Optimization 23 (2002) pp.336–346. doi:https://doi.org/10.1007/s00158-002-0194-2.

[25] Z. Jihong, Z. Weihong, Maximization of structural natural frequency with optimal support layout, Structural and Multidisciplinary Optimization 31 (2006) 462–469. doi:10.1007/s00158-005-0593-2.

[26] H. Denli, J. Sun, Optimization of boundary supports for sound radiation reduction of vibrating structures, Journal of vibration and acoustics 130 (2008). doi:https://doi.org/10.1115/1.2776345.

[27] X. Meng, T.-U. Lee, Y. Xiong, X. Huang, Y. M. Xie, Optimizing support locations in the roof–column structural system, Applied Sciences 11 (2021). URL: https://www.mdpi.com/2076-3417/11/6/2775. doi:10.3390/app11062775.

[28] Y. Zelickman, O. Amir, Optimization of plate supports using a feature mapping approach with techniques to avoid local minima, Structural and Multidisciplinary Optimization 65 (2022) pp.1–16. doi:https://doi.org/10.1007/s00158-021-03135-3.

[29] E. Reissner, The effect of transverse shear deformation on the bending of elastic plates, Journal of Applied Mechanics (1945) pp.A69–A77. doi:https://doi.org/10.1115/1.4009435.

[30] R. D. Mindlin, Influence of rotatory inertia and shear on flexural motions of isotropic, elastic plates, Journal of Applied Mechanics 18 (1951) pp.31–38. doi:https://doi.org/10.1115/1.4010217.

[31] K.-J. Bathe, Finite element procedures. ISBN: 987-0-9790049-0-2, Klaus-Jurgen Bathe, 2006.

[32] C. Européen, Eurocode 2: Design of concrete structures—Part 1-1: General rules and rules for buildings, 2004.

[33] A. Committee, Building code requirements for structural concrete (aci 318-08) and commentary, American Concrete Institute, 2008.

[34] O. C. Zienkiewicz, J. Z. Zhu, The superconvergent patch recovery and a posteriori error estimates. part 1: The recovery technique, International Journal for Numerical Methods in Engineering 33 (1992) pp.1331–1364. doi:https://doi.org/10.1002/nme.1620330702.

[35] R. H. Wood, G. S. T. Armer, , A. Hillerborg, Teh theory of the strip method for design of slabs. (includes appendix), Proceedings of the Institution of Civil Engineers 41 (1968) pp.285–311. doi:https://doi.org/10.1680/iicep.1968.7755.

[36] K. Svanberg, The method of moving asymptotes—a new method for structural optimization, International journal for numerical methods in engineering 24 (1987) pp.359–373. doi:https://doi.org/10.1002/nme.1620240207.

[37] M. B. Fuchs, M. A. Brull, A new strain energy theorem and its use in the optimum design of continuous beams, Computers & Structures 10 (1979) pp.647–657. doi:https://doi.org/10.1016/0045-7949(79)90008-7.

[38] M. Sarkisian, E. Long, A. Beghini, R. Garai, D. Shook, R. Henoch, A. Diaz, Optimal tendon layouts for concrete slabs in buildings derived through density-based topology optimization

algorithms, in: World Congress of Structural and Multidisciplinary Optimisation, Springer, 2017, pp. 1042–1053. doi:https://doi.org/10.1007/978-3-319-67988-4_79.

[39] SOM, Parkmerced - block 22, https://sfplanning.s3.amazonaws.com/default/files/publications_reports/parkmerced/21_25ChumaseroDrive-20150724.pdf, 2015. Accessed: 2018-12-06.

[40] L. He, M. Gilbert, M. Shepherd, Automatic yield-line analysis of practical slab configurations via discontinuity layout optimization, Journal of Structural Engineering 143 (2017) 04017036. doi:https://doi.org/10.1061/(ASCE)ST.1943-541X.0001700.

[41] Y. Zelickman, O. Amir, Optimization of post-tensioned concrete slabs for minimum cost, Engineering Structures 259 (2022) 114132. doi:https://doi.org/10.1016/j.engstruct.2022.114132.